Repeatability of Industrial Robots

Markus Leitner[1], John Hayes[2], Ronald Ofner[3], Christian Sallinger[4]
Department of Automation, University of Leoben
Peter-Tunner-Str. 27, A-8700 Leoben
Tel. ++43 3842 402 - 9031, Fax - 9032
Email: automation@unileoben.ac.at

July 21, 2000

[1]CD-Labor fuer Sensorische Messtechnik, Tel. ++43 3842 402 - 9046, Email: markus.leitner@unileoben.ac.at
[2]Tel. ++43 3842 402 - 9047, Email: john.hayes@unileoben.ac.at
[3]Tel. ++43 3842 402 - 9047, Email: ronald.ofner@unileoben.ac.at
[4]Tel. ++43 3842 402 - 9047, Email: christian.sallinger@unileoben.ac.at

Contents

Chapter 1

Introduction

Future robotic applications include measurement tasks (geometry measurement of parts too complicated for standard systems), flexible measurement and duplication (machining) systems or high-precision manipulating systems. In all these applications the repeatability and accuracy of the robot is of major importance to the overall performance of the system. One can simply compare the specifications of different measurement heads and robots to see the necessity of a closer look into robot specifications. The robots at our institute (KUKA KR-15/2 and Kawasaki Js-10) have a specified repeatability of ±0.1 mm (without detailed definition of environmental conditions), specifications of selected light-sectioning heads are given in the following Table. If one wants to get the full resolution of the heads for the different robot positions the influence of robot repeatability has to be considered.

Table 1.1: Range and resolution data for selected measurement heads.

Type of head	Height range /mm	Lateral range /mm	Height range /mm	Lateral range /mm
MEL M2D 8.2/5	8	5.2	0.04	0.04
MEL M2D 40/20	40	20	0.12	0.08
Custom head[1]	3.4 .. 14	3.2 .. 13	0.006 .. 0.025	0.004 .. 0.017

This report deals with the repeatability of industrial robots in general and of the KUKA KR-15/2 in particular. Typical commercial applications

[1]On the custom head the optics can be modified, therefore the range and resolution can be adapted to the task.

for industrial robots, such as spot welding, painting, assembly, packaging, palletising, etc., require that a variety of *taught* configurations be repeatable. A taught configuration is one that the manipulator is moved to physically. The joint position sensors are read and the joint angles stored. When the robot is commanded to return to that configuration from some other, each joint is returned to the stored value. Thus, *repeatability* is a measure of how precisely a robot can return to a taught point [1]. It has come to be the standard configuration performance indicator specified by manufacturers [2].

The *accuracy* of the robot is the precision with which a computed pose can be attained [1]. When required robot poses are computed off-line, external to the robot controller, the inverse kinematics of the device must be computed in order to solve for the required joint angles. It may be that the goal position and orientation is one that the robot has never before attained, hence a measure of repeatability is no longer sufficient to assess the precision of the computed pose; accuracy must be considered. This is especially true when robotic metrology tasks are guided by vision, or other motion guidance systems external to that of the robot. However, external measurement devices to determine the actual pose of the robot must be employed. Laser tracking systems to measure the pose are described in [3]. This type of interferometer measurement yields excellent accuracy compared to methods employing theodolites [4], but are less time intensive.

Another approach to vision guided robot motion and metrology is to use just relative motions of the robot and to compute the necessary motion increment from measurements. In this case the accuracy for relative motions has to be considered, but the computing of robot kinematics can be left to the robot controller as long as one is satisfied with the controller output (regarding kinematics, path planning, etc.).

In practice industrial robot manufacturers, at least those presented to the public at the Hannover 2000 Messe, give vague quantification of repeatability while virtually ignoring accuracy altogether. The specifications for repeatability are, in general, not defined with respect to other operating parameters such as temperature, joint rates and payload [5]. This renders the reported quantity as useless for comparing the performance of various robots and assessing their suitability for particular tasks. The motivation for this study arises from these problems.

Another important, but often overlook issue, is that repeatability and accuracy are not constant throughout the entire volume of the workspace.

Fluctuations arise from thermal expansion, dimension errors, dynamic characteristics and system errors of the controller inverse kinematics algorithms. Therefore, uniform methods for quantifying repeatability and accuracy over an extremely broad range of operating conditions covering the entire working envelope are required [6]. There exist detailed ISO standards for evaluation and presentation of these performance indicators [7, 8]. They should be statistically derived based upon repeated experiments covering the entire workspace [6]. Refinements in statistical analysis and modelling for performance measurement are now available in the literature, see [2, 5].

The lower bound of the accuracy of a robot is its repeatability. To obtain a reasonable *first order* estimation of the repeatability of a KUKA KR-15/2 robot, and hence the "best-case" estimation of accuracy, we have devised an experiment which allows us to quantify the repeatability in different directions (in four taught positions). The robot repeats the motion sequence for a period of about 60 hours. In each pose the robot points a laser directly onto a CCD camera chip, i.e., no lens. After visiting the four camera configurations, the robot presents itself to an infra-red camera for a temperature measurement. The experiment was run three separate times using three different maximum joint actuator motor speeds, 30, 75 and 10 % of maximum speed. The first and second runs were started with the robot at ambient room temperature. For the final run the robot was not allowed to cool down.

We approached the design of the experiment so that the results should provide information on how the individual motion of joint motors 4 and 5, as well as that of the thermal expansion of the robot links affects the ability to repeat a task. The results should be of use in planning similar cyclic tasks performed while providing information to compensate for the effects of operating conditions (temperature changes, duration of operation, maximum motor speed, etc.) on the repeatability. From the joint angles used in changing the configuration to point to the next camera and from the laser position error, we get an overall view of the repeatability in this context.

Chapter 2

Setup

2.1 Robot

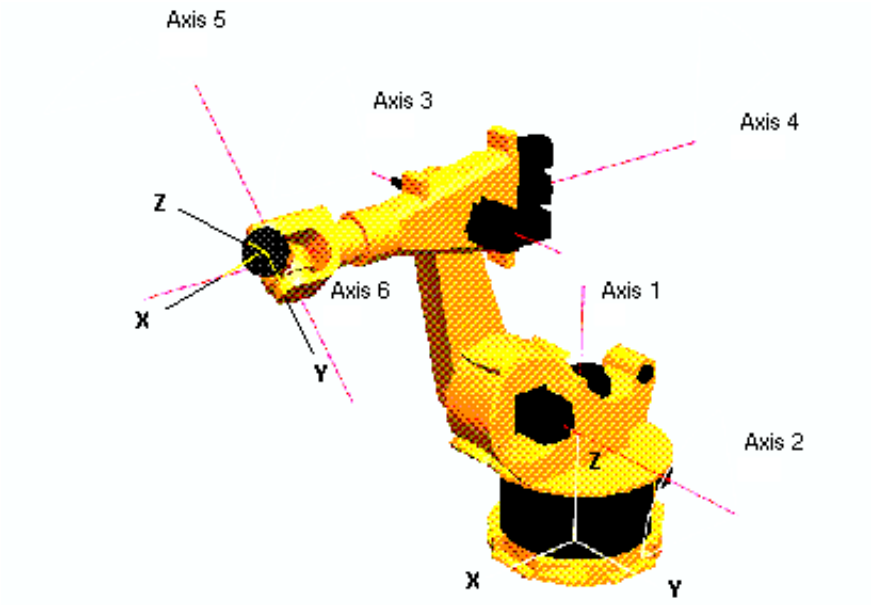

Figure 2.1: KUKA KR-15/2.

The subject of this experiment is a KUKA KR-15/2. It is a *wrist-partioned* [2] robot with six actuated revolute axes. The axes, together with the base and tool reference coordinate frames, are illustrated in Figure 2.1.

[2]Wrist-partitioning means axes 4, 5 and 6 all intersect in the same point, so positioning tasks are decoupled from orienting tasks. Hence the term *partitioned*.

Its rated payload is 15 kg and the volume of its working envelope, using the wrist-centre (intersection of orthogonal axes 4, 5 and 6) as reference point, is approximately 13.1 m^3. Detailed specifications are available on-line from http://www.kuka.de/web/re_engl/index.html. The most important specification related to this experiment is, of course, the stated repeatability:

$$\text{repeatability} \quad = \quad \pm 0.1 \text{ mm}.$$

We refer later to the robot *links*. Joint 1 permits rotation about axis 1, shown in Figure 2.1. It joins the first link to the *zeroth* link, the relatively fixed base of the robot. Joint 2 connects links 1 and 2, joint 3 connects links 2 and 3, etc.. In general, the n^{th} joint connects the $(n-1)^{st}$ to the n^{th} link, permitting relative rotation between the neighbouring links about axis n.

2.2 CCD Cameras and Laser

The measurement raw-data was obtained using the following equipment (see table 2.1).

Table 2.1: Measurement equipment.

CCD-Camera	Pulnix TM-6CN	CCIR-Norm
		Resolution: 752(H)x582(V)
		Cell size: 8.6(H)x8.3(V) μm
	Camera Adjustments	Gamma: 0.45
		Manual Gain Control
		Field Mode
		Blacklevel = 0.1 mV
		Whitelevel = 0.7 mV
Electronic shutter		1/10000 s
Laser Diode	Schaefter and Kirchhoff	Wavelength = 638 nm
		Max. output power = 11 mW
		(tuned to be almost invisible)
Framegrabber	National Instrument	PCI-1408 monochrome

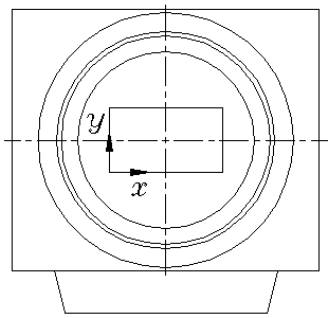

Figure 2.2: Camera image reference coordinates.

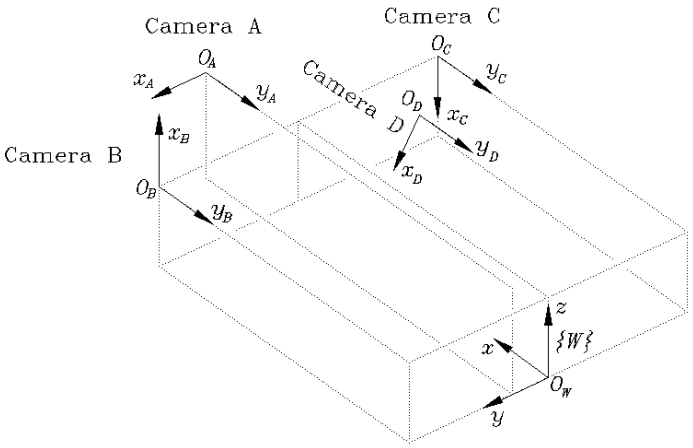

Figure 2.3: Camera Placement.

2.2.1 CCD Camera Placement

The Pulnix TM-6CN camera reference coordinate origin and basis directions directly on the CCD-chip are illustrated in Figure 2.2. This figure is a schematic drawing of the front view of the camera without any optics. The coordinates of the laser point in each of the four camera images are with respect to the corresponding camera coordinate system.

The cameras were placed so that the camera coordinate planes were constrained with respect to the *world* coordinate frame of the robot, $\{W\}$, see Figure 2.3. Frame $\{W\}$ can be located arbitrarily. We selected its position and orientation to be identical to that of the robot base frame, located

within the fixed zeroth link of the robot. Figure 2.4 shows the cameras in their mounting brackets and the measurement head mounted to the robot tool flange pointing the laser onto camera A (no camera mounted to the head).

Figure 2.4: The four cameras and laser.

The y-axis direction of all four cameras is, by design, always parallel to the x_W-axis, see Figure 2.3. The camera x-axis directions are all different, again by design, see Figure 2.3. The rational being that each of the axis directions of $\{W\}$ are covered, as well as a linear combination of y_W and z_W to give some indication of orientation error.

To get a focused image of the Laser on the chip the distance from the Laser to the CCD-chip has to be kept the same for all measurements (see Table 2.2).

Table 2.2: Distance between laser and camera flanges.

Camera	Distance (mm)
A	105
B	106
C	106
D	106

Camera A

The constraint on this camera is that the CCD chip plane be parallel to the xy-plane of the robot base frame, see Figure 2.3. Variations in the location of the coordinates of the laser point in the camera reference frame give an indication of the position error in the xy-plane of $\{W\}$.

We assume that when the robot is in this configuration the first three links[3] dominate the position error, so only the first three joint angles are significant. When the robot points the laser towards camera A, the configuration is called *pose A*. The first three joint angles are contained in Table 2.3. The length of the first three links is projected into the base plane of the robot parallel to the ground, the xy-plane, using the nominal link lengths, shown in Figure 2.5 and listed in Table 2.4 and relevant angles from Table 2.3.

Table 2.3: Joint angles for position A.

Axis	Angle°
ϑ_1	-10.3610
ϑ_2	-21.6893
ϑ_3	89.7382
ϑ_4	-2.2071
ϑ_5	0.8810
ϑ_6	-182.1840

[3]Because this is *wrist-partitioned* manipulator there are only 4 relevant link lengths. Axes 4, 5 and 6 intersect in the same point.

Table 2.4: KUKA KR-15/2 link lengths at 23°C.

Link	Length (mm)
1[4]	$\sqrt{675^2 + 300^2}$
2	805 (650+155 offset)
3	600
4	140

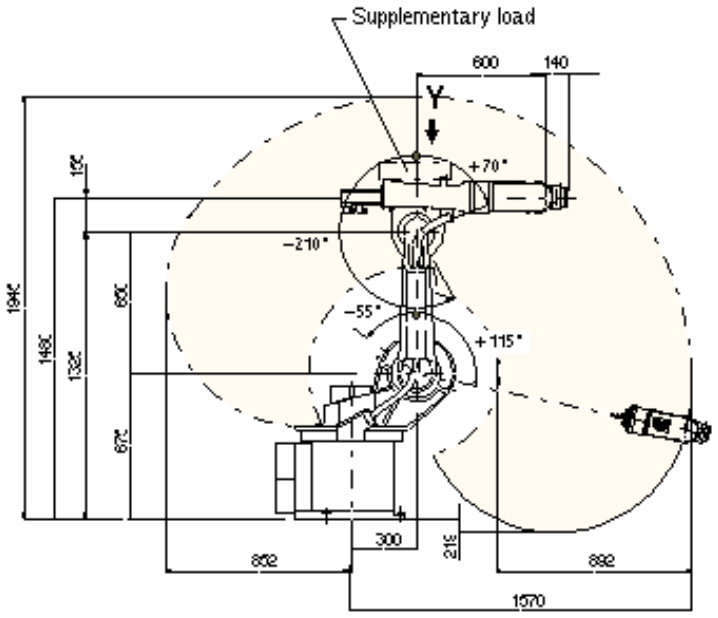

Figure 2.5: KUKA KR-15/2 nominal link lengths.

Camera B

The constraint on this camera is that the CCD chip plane be parallel to the zx-plane of the robot base frame, see Figure 2.3. Variations in the location of the coordinates of the laser point in the camera reference frame give an indication of the position error in the zx-plane of $\{W\}$.

[4]We will only be interested in the vertical and horizontal projections of link 1. These are the lengths in the xy- and zx-planes of frame $\{W\}$.

Table 2.5: Joint angles for position B.

Axis	Angle°
ϑ_1	-4.2300
ϑ_2	-17.5462
ϑ_3	106.8840
ϑ_4	-89.5300
ϑ_5	66.8551
ϑ_6	-180.0000

Camera C

The constraints on camera C are identical to those of camera B except that view plane of camera C is reflected in the zx-plane of $\{W\}$. That is, it is rotated by 180° in a point in the zx-plane. Variations in the location of the coordinates of the laser point in the camera reference frame give an indication of the position error in the zx-plane of $\{W\}$. Moreover, these errors are related to the motion of robot axis 4 only, but thermal dimension fluctuations in other links affect both camera B and C in the same way, these additional effects may be effectively subtracted out because of the camera position symmetry with respect to axis 4.

Camera D

From camera C to D axis 5 is rotated by $-9.1100°$. Thus $\boldsymbol{y}_C$ and $\boldsymbol{y}_D$ have the same direction, the $\boldsymbol{x}_D$ axis has been rotated about $\boldsymbol{y}_D$. The origin of the reference frame of camera D is on the plane spanned by the basis vectors $\boldsymbol{x}_B$ and $\boldsymbol{x}_C$, see Figure 2.3. Variations in the location of the coordinates of the laser point in the camera reference frame give an indication of the position error $\boldsymbol{x}_D$ and $\boldsymbol{y}_D$. The comparison of results of camera C and D allows us to estimate the influence of axis 4 on the repeatability.

For further interpretation of the data the relative distances between the cameras and the robot axes and the cameras themselves have to be specified (see Table 2.6).

Table 2.6: Other relative distances and angles.

Between	Measure
Camera flange B and C	600 mm
Camera flange B and axis 4	300 mm
Camera flange C and axis 4	300 mm
From axes $\boldsymbol{x}_C$ to $\boldsymbol{x}_D$ about $\boldsymbol{y}_D$	-9.1100°
Camera B and C about axis 4	179.0460°

2.3 Infra-Red Camera

Temperature measurements were obtained using an FSI FLIR SC 500 ThermoVision Uncooled Infrared Camera. Table 2.7 contains the relevant technical specifications for the camera.

Table 2.7: IR Camera.

Imaging	Field of view/min focus dist.	24°×18° built-in/0.5m
	Thermal sensitivity	0.1°C at 30°C.
Detector	Type	Focal Plane Array (FPA), Uncooled microbolometer, 320 × 240 pixels.
	Spectral range	7.5-13μm Built-in atmospheric filter with cut-on at 7.5μm.
	Temperature range	-20°C to 120°C.
	Accuracy	±2% of range or ±2°C.

Chapter 3

Experimental Results and Discussion

The measurement cycle described in Chapter 2 was carried out for three different robot speed settings (30 %, 75 % and 10 %). One can expect different speeds to result in different heat-up curves and differences in positioning dynamics.

3.1 Robot Speed = 30 % of maximum

This measurement cycle was performed by the robot changing configuration at 30 % of maximum motor speed. We judged this to be a good speed for our first experiment because it would involve lower dynamic position errors than would be encountered at higher joint velocities. With this limit on the joint rates the expectation is that the major influence on positioning error will be thermal effects exhibited during heat-up. The energy loss by the motors will be transferred to the links as heat until steady state temperature is reached.

An incidental result from the following experiments shows that without sufficient contextual information regarding heat-up the manufacturers stated repeatability has no practical meaning.

The robot was started on July 7th and performed the automatic measurement program for more than 15 hours.

Start of measurements: 7.7.2000, 20:27

End of measurements: 8.7.2000, 11:41

Resulting measurement time: 914 minutes

Ambient temperature: (23.0 ± 0.5) °C

Relative humidity: 65 - 70 %

The robot was at ambient room temperature ((23.0 ± 0.5) °C) at the beginning of the measurement run. 1068 measurement cycles were performed, at every second cycle images of the laser spot on each CCD-chip were taken and an infra-red image was recorded.

3.1.1 Determination of Pose Repeatability

The repeatability in each camera position was calculated from the positional variation of the laser spot on the CCD-chip. Based on the pixel size we expect a pixel resolution of 8.6 μm. We estimate the resolution provided by our two-dimensional COG-algorithm [9] used for the evaluation is approximately 1 μm. Raw data recorded by camera A is shown in Figure 3.1.

Figure 3.1: Raw image from camera A (image WarmUpA1022), calculated position: $x = 388.9$, $y = 317.4$.

Remark: Some difficulties were encountered with the cable of camera B. The raw images were affected by some background noise. We traced the problem to the cable. Though we were not able to repair it during the measurements the impact on the results is acceptable due to the algorithms used for evaluation. For measurement runs at 75 % and 10 % the noisy

cable was used for camera A instead of camera B. We wanted to use the differences in the results from camera C and B, and from D and C to get error information on joint axes 4 and 5. By switching cables we guaranteed the best images for this task.

At the beginning the results are dominated by the thermal effects. The heat generated by the operation of the robot causes its links to elongate, dominated by an exponential function. This can be seen from the position of the center of the laser spot over the time of the measurement (see Figures 3.2-3.5). To quantify the time constant for comparison between the different runs we fitted the curves with single-exponential decay curves (where appropriate). The results are inserted into the figures.

The camera plane coordinates are always those shown in Figure 2.2. In Figures 3.2-3.5 the left-hand vertical axis is the camera x-axis and the right-hand one is the camera y-axis. Arrows located close to the appropriate curve point to the relevant vertical axis. The horizontal axis is always time in minutes. Inserted into the figures are some results, the standard deviation at steady-state, s (s equals one sigma, σ), see below, the Range (maximum span of data in steady-state) and results of exponential fitting to the curve.

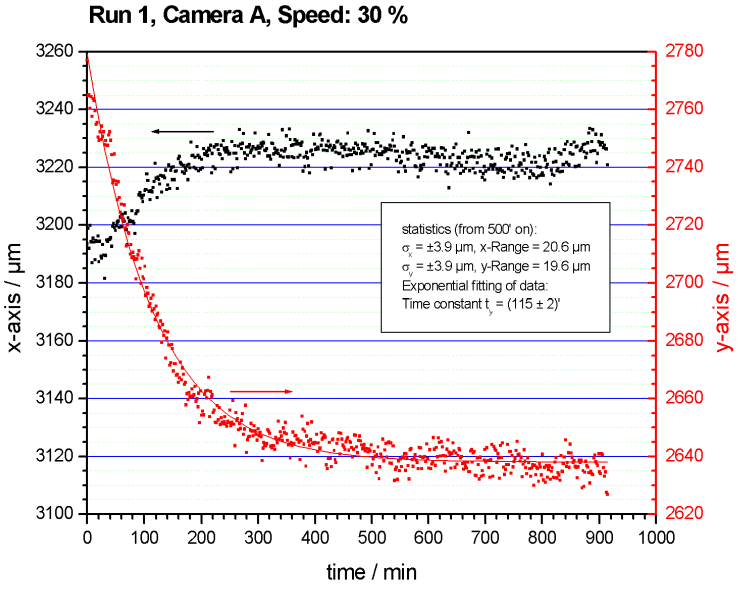

Figure 3.2: Center of laser spot on camera A over measurement time.

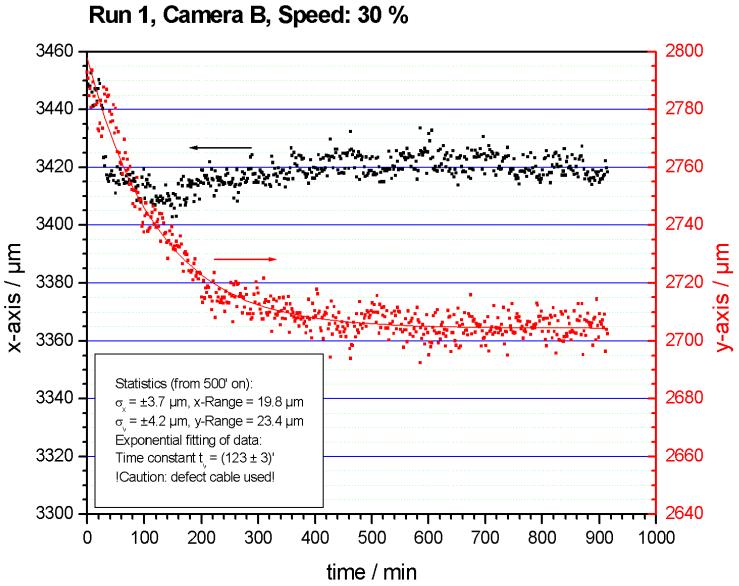

Figure 3.3: Center of laser spot on camera B versus measurement time.

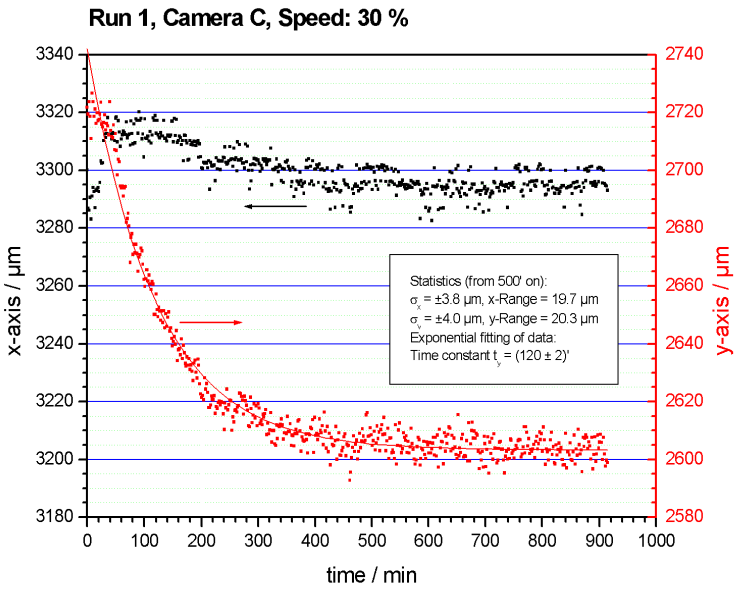

Figure 3.4: Center of laser spot on camera C versus measurement time.

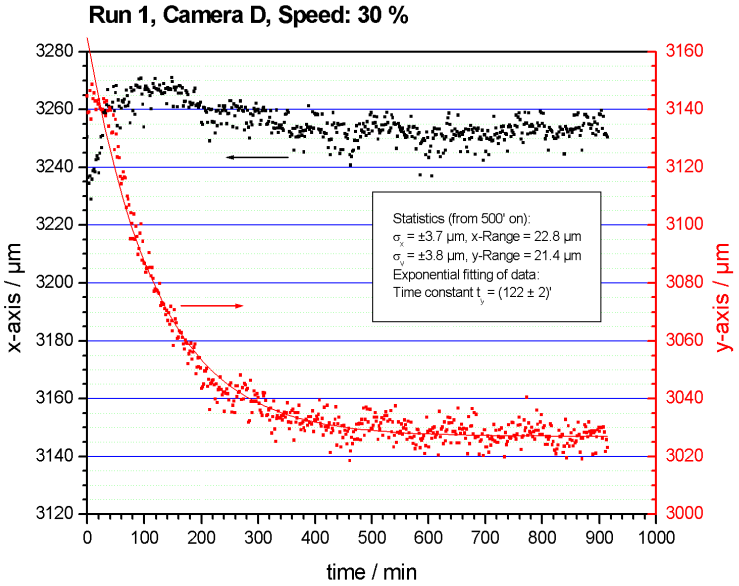

Figure 3.5: Center of laser spot on camera D versus measurement time.

As can be seen, the change in position shows exponential behaviour with a time constant of between 115-120 minutes (the time constant being the time it takes to reach $(e-1)/e \approx 63\%$ of steady state). It takes approximately 300 minutes until the repeatability remains within the range of 30 to 40 μm. Steady state seems to be attained in about 500 minutes after start. To quantify the repeatability in this steady state we calculated the standard deviation and minimum/maximum deviation from 500 minutes until the end of the run. These results are inserted into figures 3.2 - 3.5.

Based on these results we conclude that the steady state means a standard deviation of ± 4 μm (1 σ) or ± 12 μm (3 σ) in all recorded directions with maximum variations of 20 to 30 μm (3 σ are stated here because this is the value the ISO9283 [7] defines to be given for the position repeatability). Note, this is a significant improvement on the manufacturer reported repeatability of ± 100 μm (± 0.1 mm). However, if warm-up deformation is included the maximum variation is on the order of 141 μm, but this is unidirectional. According to ISO9283 [7], the actual repeatability would then be on the order of ± 140 μm, significantly worse than $\pm 100 \mu$m.

In Table 3.1 the approximate overall y-range in position from the start of run 1 till the end, as estimated from Figures 3.2 - 3.5, are listed. They will

be used for comparison with runs 2 and 3.

Table 3.1: y-range in positions for run 1.

Camera A (μm)	Camera B (μm)	Camera C (μm)	Camera D (μm)
141	105	132	129

In the next section we compare these results with the infra-red images taken during the first measurement run to track down the source of the thermal shift evident within the first 500 minutes.

3.1.2 Measurement of robot temperature

We recorded the temperature of the robot during the measurement run with the infra-red camera. Color-coded thermal images are shown in Figures 3.6 and 3.7. Note, the hot spot visible on the nearly vertical arm of the robot in Figure 3.6 is the laser power supply.

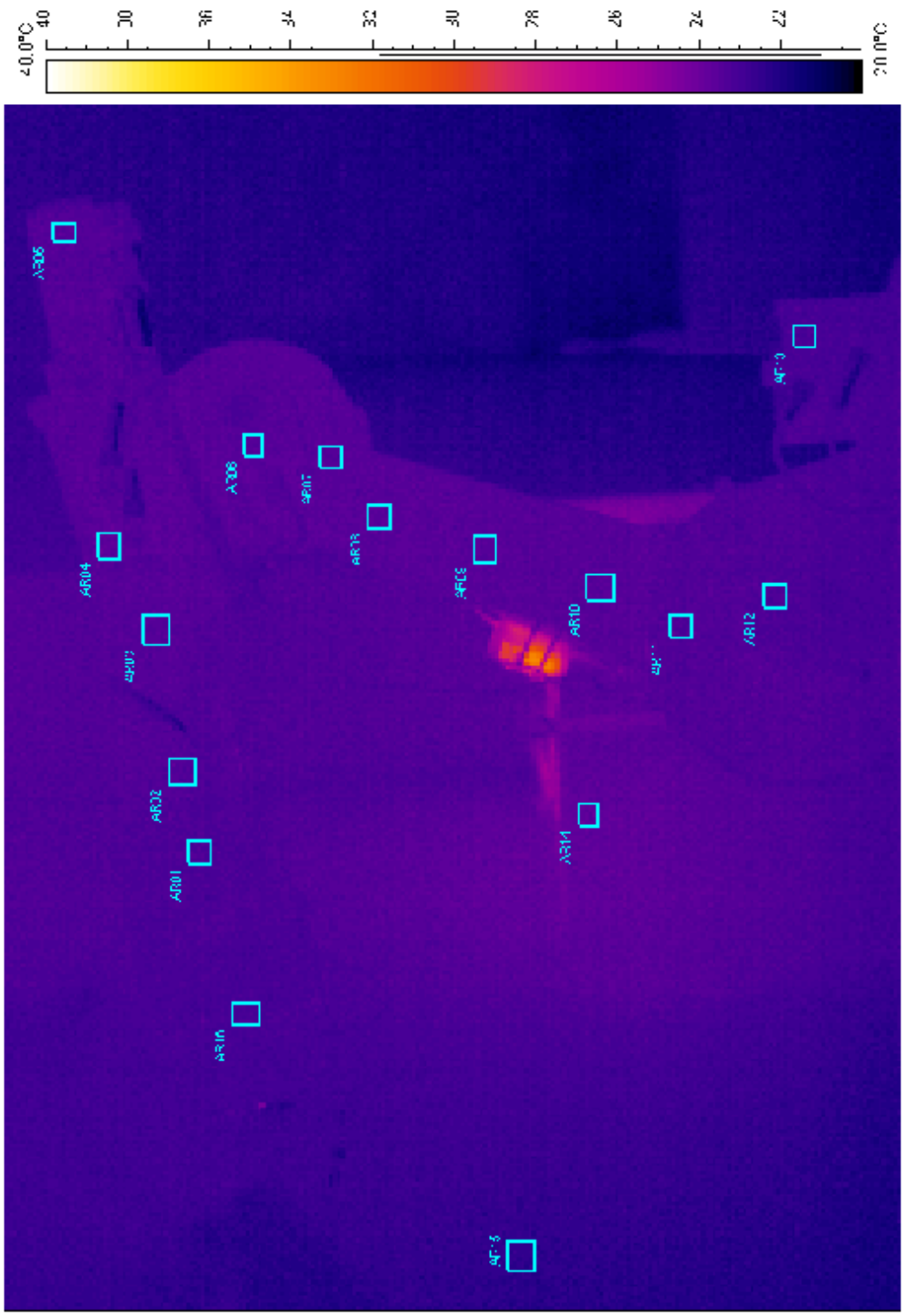

Figure 3.6: Temperature of robot at beginning of measurements.

Figure 3.7: Temperature of robot at end of measurements.

The rectangles AR01 - AR16 seen in these two figures show the regions that we chose for a deeper analysis of the change of temperature with time. Within each rectangle the average temperature was calculated (compared to the temperature at a single pixel which gives better resolution). The resulting values are then presented in Figures 3.8 - 3.10. Figure 3.8 contains the spots of the end effector part, Figure 3.9 those of the middle part of the robot and 3.10 those of the robot base and controller. In each figure the room temperature is plotted for reference.

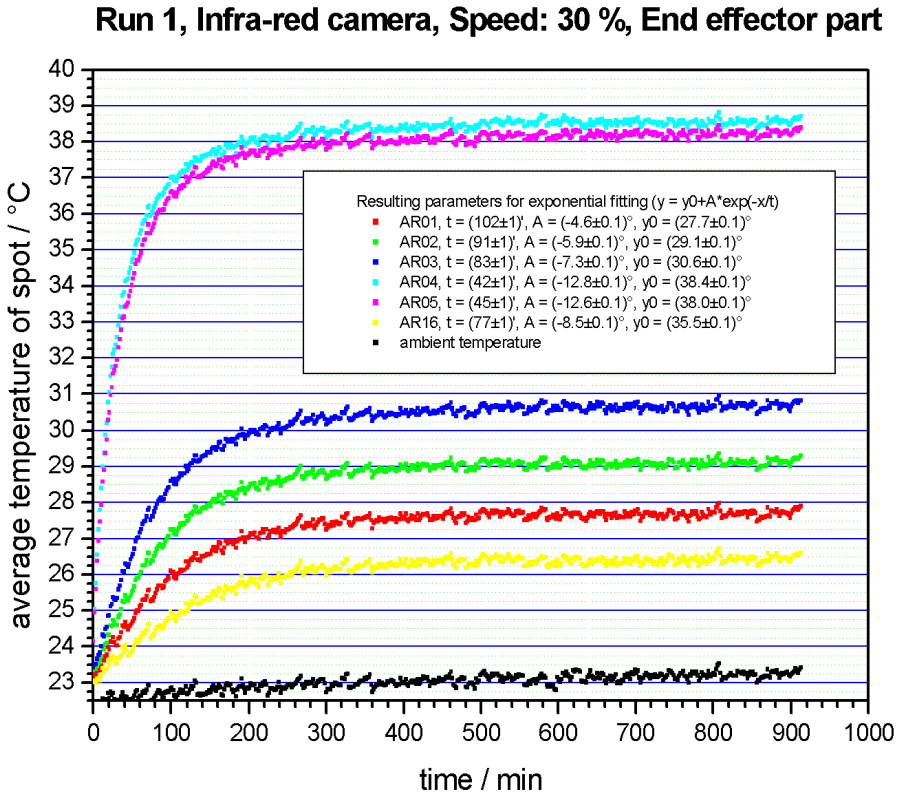

Figure 3.8: Average temperature at measurement spots on end effector and lower arm.

As one can see there is noise on each measurement with the same fingerprint (systematic noise). This reflects the limited absolute accuracy of the infra-red camera and can be improved by measuring a reference temperature and linking the data to this reference. However, for this experiment we are

only interested in temperature differences and the accuracy is sufficient for our task. The additional temperature reference is therefore unnecessary.

The curves in Figures 3.8, 3.9 and 3.10 clearly demonstrate exponential behaviour. We fitted a single exponential function to each curve. The results are inserted into the figures.

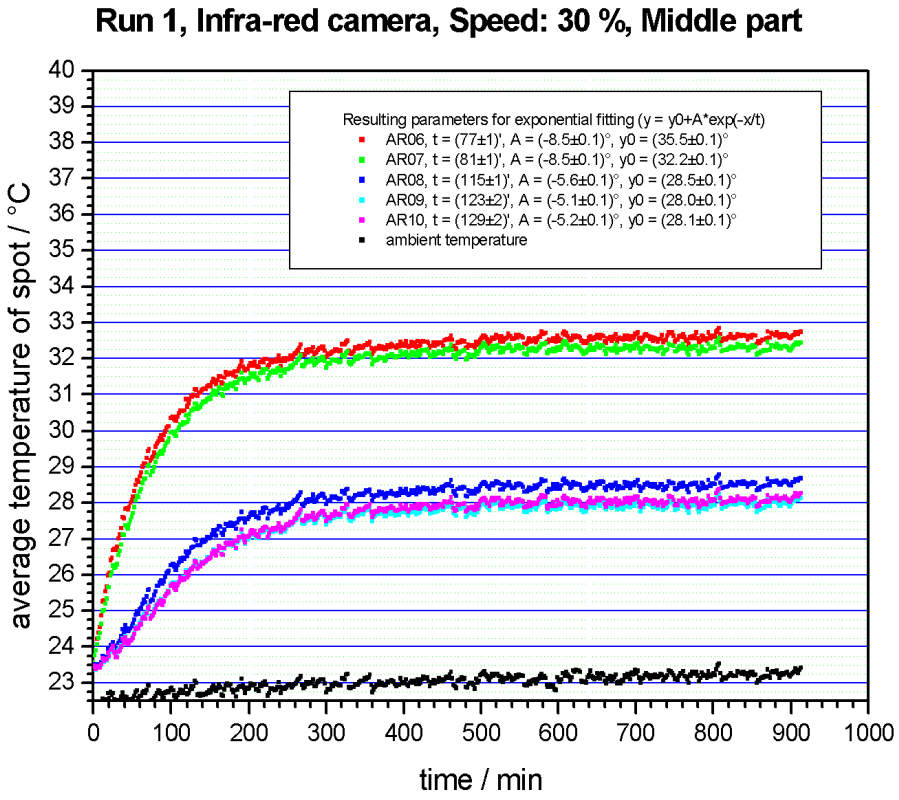

Figure 3.9: Average temperature at measurement spots on middle part of robot.

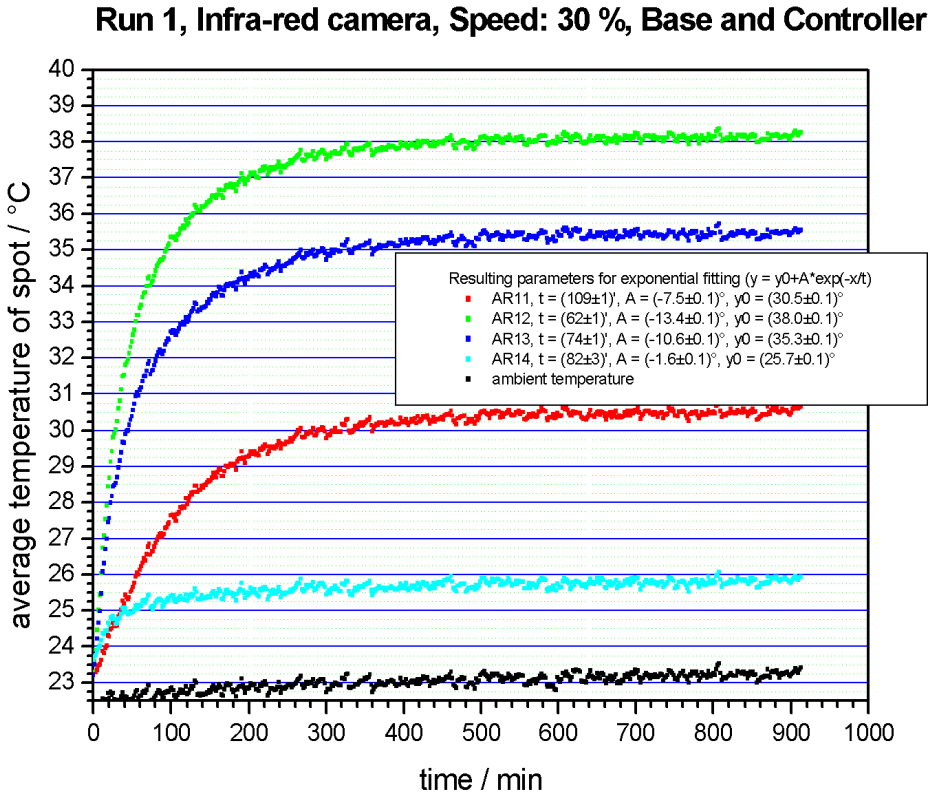

Figure 3.10: Average temperature at measurement spots on robot base and controller.

3.1.3 Interpretation of Position Error Due to Thermal Expansion in the Camera Planes

In the following we estimate the thermal expansion of the robot arm in the various camera coordinate directions, illustrated in Figure 2.3, based on the infra-red data. These data show the heat-up to be between 4.6 - 7.3 °C for the links and 12.6 - 12.8 °C for the motors.

The cameras show link elongation of approximately 105 - 140 μm in the results of camera A, C and D. The data for camera B should be treated with a measure of skepticism due to the noisy cable, but these results seem to be smaller compared to the other three cameras, particularly in the y_B direction.

Recall that the y-axis directions of all four cameras are always parallel to the x_W-axis, see Figure 2.3. It is noteworthy that these position errors exhibit strong exponential function behavior. This exponential function is strongly related to the exponential heat-up function. The implication is that in the x_W-axis direction the position error is always dominated by thermal effects.

The camera x-axis directions are all different, see Figure 2.3. The x-axis data in Figures 3.2-3.5 is initially exponential in behavior but then appears to have a small drift. This indicates that in these coordinate axis directions the heating effect of the first two links is initially dominant, but is subsequently eclipsed by other sources of error. These may also be thermal in nature, but are more complicated than the first order model we assumed.

Camera A

Laser spot positioning errors measured along the x_A- and y_A-axes are dominated by changes in the length of line l illustrated in Figure 3.11. Temperature changes should have a more pronounced effect on long slender links, such as links 2 and 3, than on short and stout ones, such as link 1. We assume the elongation due to temperature of link 1 will be insignificant compared to links 2 and 3. Therefore, we compute the length of l using the nominal link lengths from Table 2.4 at 23.5°C by

$$\begin{aligned} l &= \|l_2 \cos(\pi + \vartheta_2) + l_3 \cos(\pi + \vartheta_2 + \vartheta_3)\| \\ &= \|805 \cos(158.311) + 600 \cos(248.049)\| \\ &= 972.296 \text{ mm.} \end{aligned} \tag{3.1}$$

Note, the additional argument of π is necessary because the KUKA controller measures angles in a left-handed sense. This can be verified by careful examination of Figure 2.1.

An examination of Figure 3.11 reveals that an elongation of l means that the coordinates of the laser spot, S, will increase in the x_A direction and decrease in the y_A direction for this configuration, listed in Table 2.3. From that table, $\vartheta_1 = -10.3610°$. The magnitudes of the projections along the axes of frame $\{W\}$ are simply

$$\begin{aligned} l_x &= l \cos 10.3610 = 956.442\text{mm}, \\ l_y &= l \sin 10.3610 = 174.867\text{mm}. \end{aligned} \tag{3.2}$$

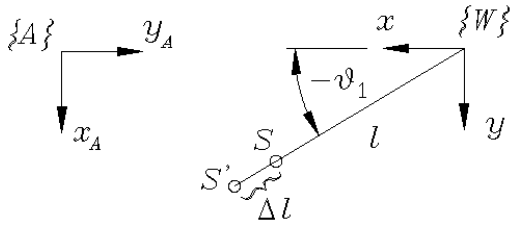

Figure 3.11: Projection of first 2 link lengths into camera A plane.

We compute a *back-of-the-envelope* analytic estimate of the expected link length deformation due to temperature using the coefficient of expansion for steel, α,

$$\begin{aligned} \Delta l_x &= l_x \alpha \Delta K, \\ \Delta l_y &= l_y \alpha \Delta K. \end{aligned} \tag{3.3}$$

The temperature data was all obtained from the IR camera images. The start temperature of 23.5°C is estimated from the image in Figure 3.6. The average overall temperature change in links 2 and 3 at the end of the run is estimated to be 34.1°C by averaging the temperatures in rectangles AR03, AR04, AR05, AR06, AR09, AR11, AR12 from the image in Figure 3.7. The overall change in temperature in links 2 and 3 is $\Delta K = \Delta°\text{C} = 34.1 - 23.5 = 11.1K$. The coefficient of expansion is taken from [10] to be $\alpha = 11.7 \times 10^{-6}\text{m/m}K$. Using these values, together with the projections of l from Equation (3.2), into Equation (3.3) gives

$$\begin{aligned} \Delta l_x &= 0.124 \text{ mm}, \\ \Delta l_y &= 0.023 \text{ mm}. \end{aligned} \tag{3.4}$$

The quantities in Equation (3.4) are with respect to frame $\{W\}$, we want them in frame $\{A\}$, the coordinate frame of camera A, see Figure 3.11. This transformation simplifies for length differences to

$$\begin{aligned} \Delta x_A &= \Delta y, \\ \Delta y_A &= -\Delta x. \end{aligned} \tag{3.5}$$

Transforming the components in Equation (3.4) with Equations (3.5) gives

$$\begin{aligned} \Delta l_{x_A} &= 0.0237 \text{ mm}, \\ \Delta l_{y_A} &= -0.124 \text{ mm}. \end{aligned} \tag{3.6}$$

The components given by Equation (3.6) give a rough approximation of the expected position error recorded by camera A due to changes in link temperature. We can now compare these values to those obtained in run 1 for the same camera reported in Figure 3.2. The comparison is listed in Table 3.2 there is a 57.2% difference for the x_A coordinates and an 11.9% difference in y_A. The important observation is that the calculated values account only for thermal effects, not dimension, dynamic or system errors. The fact the experimental position deviations are larger than the calculated ones are consistent with this observation. Moreover, it suggests that thermal effects are the dominant source of position error.

Table 3.2: Camera A: calculated and experimental deviations.

Calculated (mm)	Experimental (mm)	% difference
$\Delta x_A = 0.023$	$\Delta x_A = 0.053$	57.2
$\Delta y_A =$ -0.124	$\Delta y_A =$ -0.141	11.9

Thoughts on the interpretation of these results (also apply to the results of camera B to D, Tables 3.3 to 3.5): It has to be emphasized that the deviations in x are close to the repeatability values measured and therefore the significance of these values is smaller than the results for y. The effect of neglecting link 1 also reduces the calculated value and one has to use some precaution regarding the average temperature used (for a more thorough analysis temperature averaging over smaller segments has to be used). For the material we used a coefficient of expansion for standard steel and may be different from that of the actual material, which is not specified by the robot manufacturer.

Camera B

For this configuration the plane of camera B is parallel to the zx-plane of $\{W\}$, see Figure 2.3. We are interested in determining the projection of l into these parallel planes. Examining Figure 3.12 we see that the projection of l into the zx-plane is

$$\begin{aligned} l_{W_z} &= l\cos\varphi, \\ l_{W_x} &= l\sin\varphi\cos\left(-\vartheta_1\right). \end{aligned} \tag{3.7}$$

To compute the components in Equation (3.7) we must first compute l in

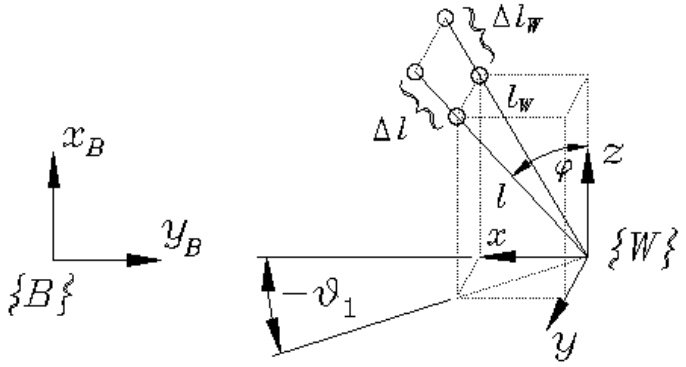

Figure 3.12: Projection of first 2 link lengths into camera B plane.

the plane containing links 2 and 3. For this we use the nominal link lengths and joint angles found in Tables 2.4 and 2.5, respectively. We obtain

$$\begin{aligned} l_z &= l_2 \cos(90 + \vartheta_2) + l_3 \cos(90 + \vartheta_2 + \vartheta_3) \\ &= 805 \cos(72.454) + 600 \cos(179.338) \\ &= -357.2728, \\ l_x &= l_2 \sin(90 + \vartheta_2) + l_3 \sin(90 + \vartheta_2 + \vartheta_3) \\ &= 805 \sin(72.454) + 600 \sin(179.338) \\ &= 774.4811, \\ l &= \sqrt{l_z^2 + l_x^2} = 852.916 \text{ mm}. \end{aligned} \tag{3.8}$$

The angle l makes with respect to the z axis, φ, is

$$\varphi = \text{atan2}(-357.273, 774.481) = 114.7642^\circ$$

The projection into the zx-plane is obtained from Equation 3.7:

$$\begin{aligned} l_{W_z} &= l_z = -357.273 \\ l_{W_x} &= 852.916 \sin(114.7642) \cos(4.2300) = 772.3712 \end{aligned} \tag{3.9}$$

Finally, the projection is

$$l_W = \sqrt{-357.273^2 + 772.371} = 851.000 \text{ mm}. \tag{3.10}$$

To compute the elongation due to temperature, we use the same temperature difference obtained for camera A, $\Delta K = 11.1K$, and expansion

coefficient, $\alpha = 11.7 \times 10^{-6}\text{m/m}K$, as inputs to Equation (3.3), together with l_{W_z} and l_{W_x}:

$$\begin{aligned} \Delta l_{W_z} &= (-357.273)(11.1)(11.7 \times 10^{-6}) = -0.046 \text{ mm}, \\ \Delta l_{W_x} &= (772.371)(11.1)(11.7 \times 10^{-6}) = 0.100 \text{ mm}. \end{aligned} \tag{3.11}$$

The transformation to the camera B plane is

$$\begin{aligned} \Delta x_B &= \Delta z_W, \\ \Delta y_B &= -\Delta x_W. \end{aligned} \tag{3.12}$$

Transforming the components in Equation (3.11) with Equations (3.12) gives

$$\begin{aligned} \Delta l_{x_B} &= -0.046 \text{ mm}, \\ \Delta l_{y_B} &= -0.100 \text{ mm}. \end{aligned} \tag{3.13}$$

We now compare the computed elongation due to temperature to the position deviation recorded by camera B. As previously mentioned, these data should be treated with some suspicion because of the noisy cable.

Table 3.3: Camera B: calculated and experimental deviations.

Calculated (mm)	Experimental (mm)	% difference
Δx_B = -0.046	Δx_B = -0.039	19.0
Δy_B = -0.100	Δy_B = -0.105	4.5

Examining the data in Table 3.3 identical statements can be made as those regarding the position error for camera A, with the proviso associated with camera B data stemming from the noisy cable.

Camera C

To move between pose B and pose C only joint angle 4, ϑ_4, is changed. This means that the computations to determine l and project it into the zx-plane of $\{W\}$ is the same as for camera B. Indeed, even the computed values for the components of Δl are identical. Only the camera C data and associated transformation from $\{W\}$ to $\{C\}$ is different. This is given by

$$\begin{aligned} \Delta x_C &= -\Delta z_W, \\ \Delta y_C &= -\Delta x_W. \end{aligned} \tag{3.14}$$

Transforming the components in Equation (3.11) with Equations (3.14) gives

$$\begin{aligned} \Delta l_{x_C} &= 0.046 \text{ mm}, \\ \Delta l_{y_C} &= -0.100 \text{ mm}. \end{aligned} \tag{3.15}$$

Table 3.4 compares the computed elongation due to temperature to the position deviation recorded by camera C.

Table 3.4: Camera C: calculated and experimental deviations.

Calculated (mm)	Experimental (mm)	% difference
$\Delta x_C = 0.046$	$\Delta x_C = 0.020$	132.0
Δy_C = -0.100	Δy_C = -0.132	24.0

Camera D

The task now is to project l from $\{W\}$ into $\{D\}$, where $\{D\}$ is inclined with respect to $\{W\}$ by joint angle 5, ϑ_5. Frame $\{D\}$ is rotated about y_C, see Figure 2.3. There is an additional translation which is unimportant since only magnitude differences are required. The axis of joint 5 in pose 3 is parallel to y_C. Only joint angle 5 is changed to bring the robot into pose 4, hence axis 5 remains parallel to y_C. The required transformation, Equation (3.16), requires only the cosine of the change of this angle, $\cos \Delta\vartheta_5$. Joint angle 5, $\Delta\vartheta_5$, was selected to be -9.110°, as listed in Table 2.6.

$$\begin{aligned} \Delta x_D &= \Delta x_C \cos \Delta\vartheta_5, \\ \Delta y_D &= \Delta y_C. \end{aligned} \tag{3.16}$$

Transforming the components given by Equation (3.15) with Equation (3.16) gives

$$\begin{aligned} \Delta l_{x_D} &= 0.046 \text{ mm}, \\ \Delta l_{y_D} &= -0.100 \text{ mm}. \end{aligned} \tag{3.17}$$

Table 3.5 compares the computed elongation due to temperature to the position deviation recorded by camera D.

Table 3.5: Camera D: calculated and experimental deviations.

Calculated (mm)	Experimental (mm)	% difference
$\Delta x_D = 0.046$	$\Delta x_D = 0.031$	47.7
Δy_D = -0.100	Δy_D = -0.129	22.2

From Table 3.5 it is clear that the thermal expansion of links 2 and 3 are, at least in the x_D direction, is no longer the dominate source of repeatability deviation.

3.1.4 Steady State Position Errors

As mentioned earlier, we estimate the time needed to reach steady state link temperature and position error is approximately 500 minutes for each camera. The temperature time constant was estimated to be between $110 < \tau < 120$ minutes from Figure 3.9. The error analysis performed on the data plotted in Figures 3.2-3.5 gives time constants for each position error ranging from 115 to 123 minutes. The natural conclusion is that there is a strong link between changes in temperature and changes in laser spot position in each camera. The time constant comparison is listed in Table 3.6.

Table 3.6: Time constants (in minutes).

Fig. 3.9	Fig. 3.2	Fig. 3.3	Fig. 3.4	Fig. 3.5
$110 < \tau < 120$	$\tau = 115 \pm 2$	$\tau = 123 \pm 2$	$\tau = 120 \pm 2$	$\tau = 122 \pm 2$

The corresponding steady state errors are listed in Table 3.7. For these positioning tasks the repeatability is nearly an order of magnitude better than that reported by the manufacturer once steady state operating temperature has been attained.

Table 3.7: Range of steady state variations (after 500 minutes).

Fig. 3.9, AR08	Fig. 3.2	Fig. 3.3	Fig. 3.4	Fig. 3.5
5.2 °	19.6μm	23.4μm	20.3μm	21.4μm

3.1.5 Discussion

This run of measurements shows that the robot complies with the specifications given by the manufacturer - if one allows it to heat up properly. The variations in pose repeatability are factor 8 better than the ±0.1 mm given by the manufacturer if the robot is allowed to heat up for 8 hours at 30% of the maximum speed (if the wait times that we needed for the images to be taken can be shortened the heat-up time should be correspondingly reduced). The work the robot carried out during heat-up has to be of the same type (same motion characteristics) and of the same frequency as the work it has to carry out afterwards.

It can be said that the shift of end-effector position with time is largely caused by the heat-up, the time constants of the shift and of the thermal data show good correspondence. The time constants indicate dominance by the effect of the middle part of the robot, i.e., links 2 and 3. Indeed, there is good agreement between the time constants from Figure 3.9 ($\tau \approx 117$ minutes) and those reported in Figures 3.2-3.5 ($115 < \tau < 123$ minutes).

3.2 Robot Speed = 75% of maximum

For run 2 of the experiment the maximum motor speed was increased to 75% of maximum. We assume that motor friction losses are proportional to velocity. Therefore, increasing the joint rates allows us to investigate the change in time constants involved in achieving a possibly higher steady temperature and hence greater thermal deformation over a shorter period of time. Based on the results from run 1 we conclude that an increase in steady state temperature implies an increase in thermal deformation. The deformation will be revealed by the difference in position of the laser spot at the beginning of the experiment and at steady state. We therefore deem it unnecessary to consider the temperature data for subsequent runs.

The following data corresponds to the start of run 2:
Start of measurements: 8.7.2000, 14:46
End of measurements: 9.7.2000, 15:06
Resulting measurement time: 1460 minutes
Ambient temperature: (23.0 ± 0.5) °C
Relative humidity: 65 - 70
Due to three hours of break between run 1 and run 2 the robot cooled

to room temperature (approx. (23.0 ± 0.5) °C) by the beginning of the measurement run 2. 2072 cycles were carried out by the robot, every second cycle images of the laser spot on each of the 4 monochrome cameras were taken and an infra-red image was recorded.

The position of the center of the laser spot recorded by each camera over the time of the measurement is shown in Figures 3.13-3.16.

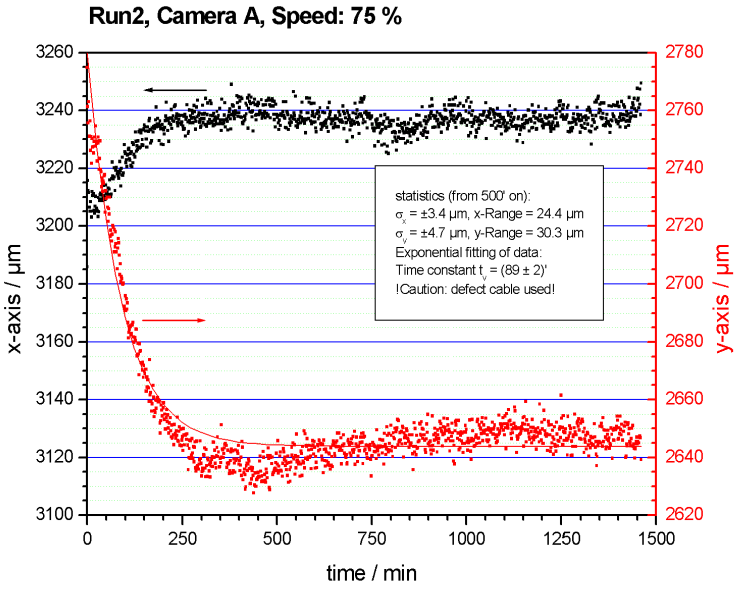

Figure 3.13: Run 2: Center of laser spot on camera A over measurement time.

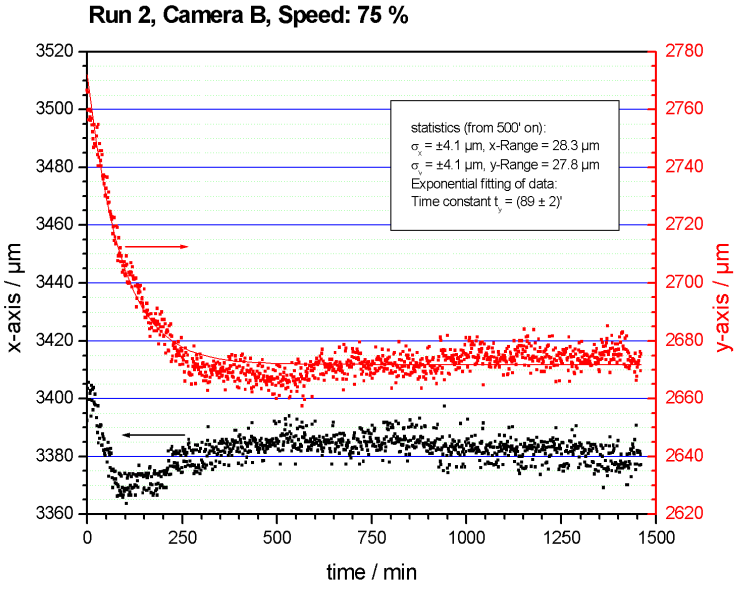

Figure 3.14: Run 2: Center of laser spot on camera B over measurement time.

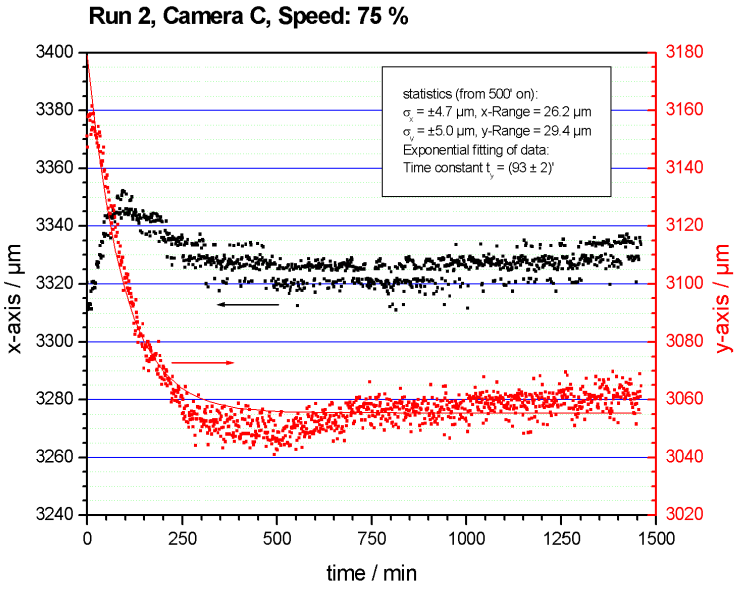

Figure 3.15: Run 2: Center of laser spot on camera C over measurement time.

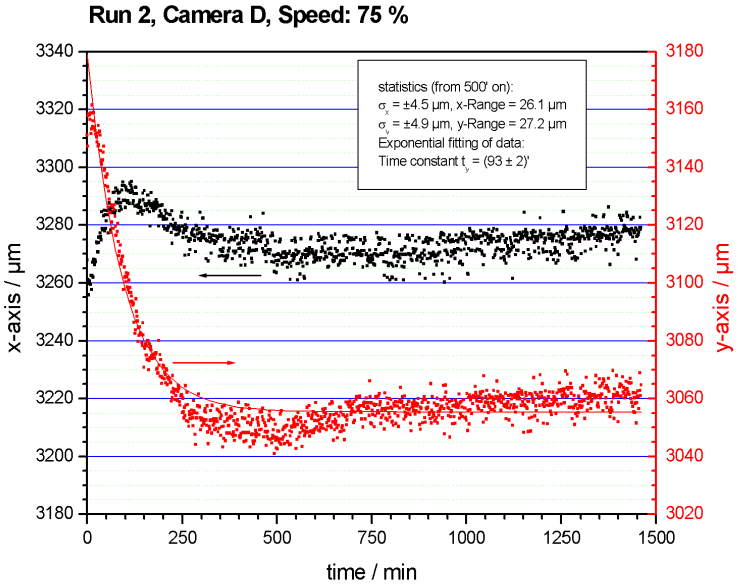

Figure 3.16: Run 2: Center of laser spot on camera D over measurement time.

3.2.1 Discussion

Comparing the overall laser spot position deviations from the start of run 2 until steady state, see Table 3.1, to the results from run 1, see Table 3.8, we see little difference. This appears to contradict our expectation that the increased motor speed should produce higher temperatures, hence greater elongations of the links. However, the communication programme between the robot controller and separate PC with the frame grabber required wait times of 6 seconds between robot motions (used mainly for image grabbing and writing data). The wait times were the same for all 3 measurement runs. This may have had the effect of allowing some of the heat caused by the friction losses to be transferred during the wait time from the robot links to the environment through natural convection and radiative heat transfer. We estimate the wait times comprised about 80 % of the entire run time.

Table 3.8: y-range in positions for run 2.

Camera A (μm)	Camera B (μm)	Camera C (μm)	Camera D (μm)
148	108	121	120

The most obvious effect of the increased motor speed was on the time constants. For quick reference, the time constants (in minutes) required to reach 63 % of steady state position variation from Figures 3.2-3.5 and Figures 3.13-3.16 are summarised in Table 3.9.

Table 3.9: Position variation time constants (in minutes) for runs 1 and 2.

Run 1	$\tau_A = 115 \pm 2$	$\tau_B = 123 \pm 2$	$\tau_C = 120 \pm 2$	$\tau_D = 122 \pm 2$	$\tau_{\text{ave}} = 120$
Run 2	$\tau_A = 89 \pm 2$	$\tau_B = 89 \pm 2$	$\tau_C = 93 \pm 2$	$\tau_D = 93 \pm 2$	$\tau_{\text{ave}} = 91$
% Diff	22.6	27.6	22.5	23.8	ave: 24.2

Averaging the time constants and % difference in Table 3.9 we see that by increasing the maximum motor speed to 75 % we achieve steady state repeatability nearly 25 % faster. The standard deviations vary from a low of $s_{x,y} = \pm 3.9\mu$m for camera A in run 1 to a high of $s_y = \pm 5.0\mu$m for camera C in run 2 (see statistics in Figures 3.2-3.5 and Figures 3.13-3.16).

3.3 Robot Speed = 10% of maximum

For this final run, run 3, we wished to observe the effects of reducing motor speed from 75 % to 10 % of maximum without allowing the robot to cool to ambient temperature. We rationalised that the speed reduction would have two major effects. First, the reduced speed would reduce the steady state temperatures of the links thereby causing the link lengths to contract; second, dynamic effects would be reduced. As with run 2, we use the results of run 1 to correlate temperature change to change in positioning variation, hence we present no temperature data.

The following data corresponds to the start of run 3:

Start of measurements: 9.7.2000, 15:10

End of measurements: 10.7.2000, 11:58

Resulting measurement time: 1248 minutes

Ambient temperature: (23.0 ± 0.5) °C

Relative humidity: 65 - 70

914 cycles were carried out by the robot, as before every second cycle images of the laser spot at the position of the monochrome cameras were taken and an infra-red image was recorded.

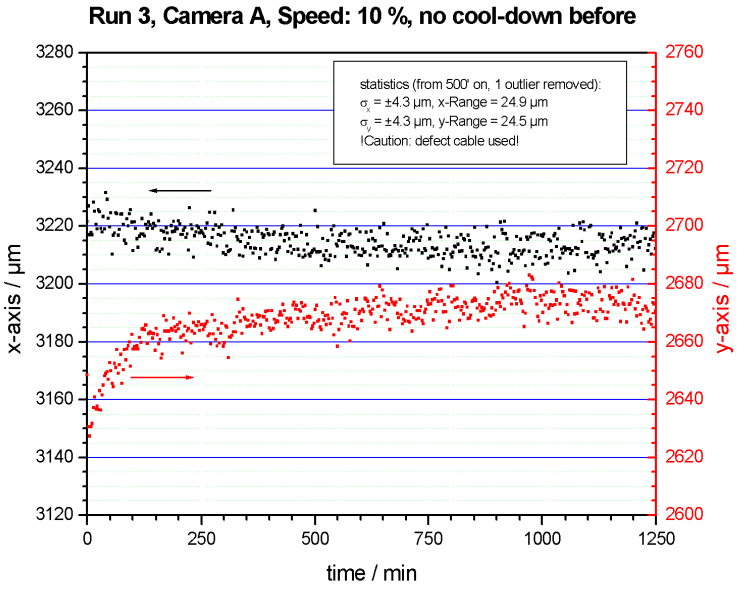

Figure 3.17: Run 3: Center of laser spot on camera A over measurement time.

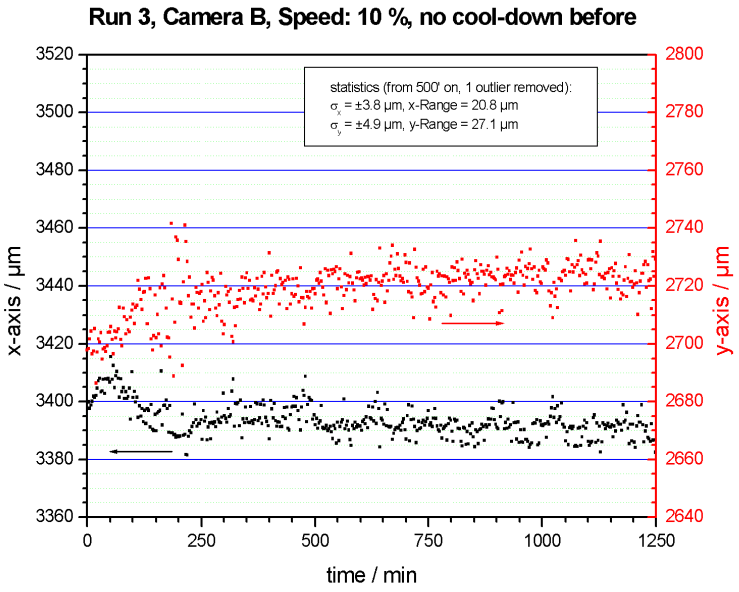

Figure 3.18: Run 3: Center of laser spot on camera B over measurement time.

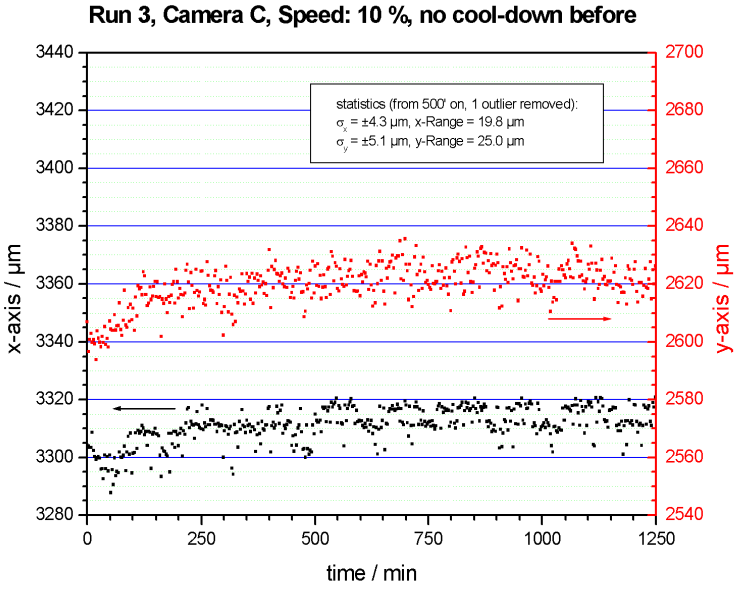

Figure 3.19: Run 3: Center of laser spot on camera C over measurement time.

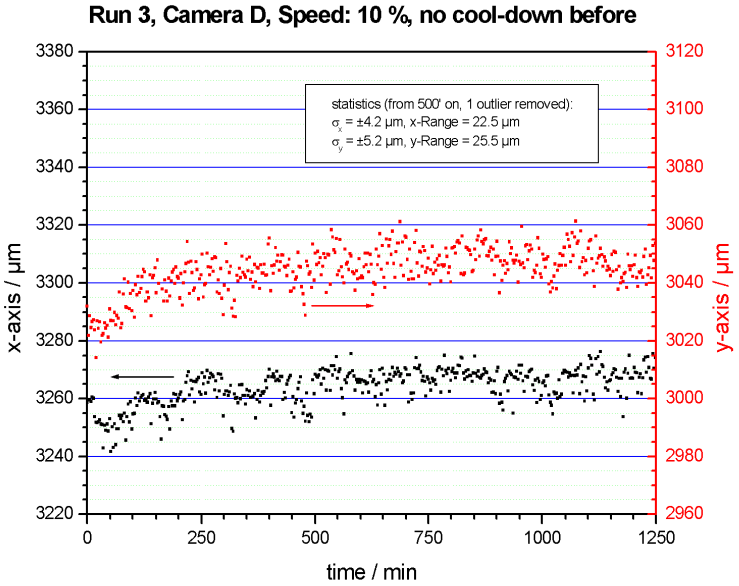

Figure 3.20: Run 3: Center of laser spot on camera D over measurement time.

3.3.1 Discussion

Measurement run 3 was started immediately after run 2, therefore there was no explicit heating up period. But due to the different speed the robot cooled down at the beginning of this run, as can be seen in the following Figures 3.17-3.20. The effect is most pronounced for cameras A, C and D. For instance, comparing Figures 3.2-3.5 to Figures 3.17-3.20 one sees that the exponential decay on the y-axis changes to exponential increase. As mentioned in Section 3.1.3, an increase on the camera y-axis corresponds to a decrease in link length in the y_W-axis direction (a decrease on the camera y-axis corresponds to an increase in link length in the y_W-axis direction).

We did not compute the time constants because the exponential behaviour in Figures 3.17-3.20 seems far less than in the previous two runs. We are therefore doubtful about the usefulness of computing and comparing time constants for run 3. It is enough, for our purposes, that we see the effects of decreasing motor speed with no chance for the links to cool ultimately results in contraction.

Comparing the statistics in the figures, there is no appreciable difference

in the steady state x and y ranges nor in the standard deviations. However, we see that the total y ranges from start to end are on the order of one half of those for either of runs 1 or 2

Table 3.10: y-range in positions for run 3.

Camera A (μm)	Camera B (μm)	Camera C (μm)	Camera D (μm)
55	50	40	46

Chapter 4

Conclusions

Results from our experiment support the claim that there is a significant positional shift over the course of cyclic operation for many hours. Furthermore, the changes are different in robot base coordinate axis directions. Evidence suggests that this phenomenon is strongly linked to the motor energy losses, transferred as heat to the robot links. When the temperature of the robot links approach steady state, so does the position repeatability. Indeed, the time constants for temperature change and position error change (computed only for runs 1 and 2) are all approximately equal. The change in position error exhibits first order exponential behavior in the x_W-axis (the y-axes of the cameras). The assumption that thermal expansion is more pronounced longitudinally than radially is supported by this result. The effect is more complicated in the other directions and in fact these deviations are much smaller and therefore less significant.

Once the robot has warmed-up, the repeatability of positioning the laser spot in each of the 4 cameras was nearly one order of magnitude better than the manufacturers stated repeatability of ± 0.1 mm. However, if the heat-up effects are ignored, the actual repeatability is closer to ± 0.2 mm, nearly double the catalogue specified value. It is noteworthy that no mention of such heating effects on robot performance can be found in the manufacturer supplied operating literature for the KUKA KR-15/2 [11].

The implication of these results is that if the thermal response of the robot for specific cyclic tasks is known, the expansion can be numerically compensated for by the controller, eliminating the need to allow the robot to heat-up. Additional possibilities for correction arise by employing measurement of robot temperature (using discrete sensors mounted to the robot

links or contact-less infra-red systems) and use of an appropriate heat-up model. If the task to be done allows, a first order calibration by presenting the robot head to a camera or measuring a calibration object with the head could significantly reduce deviations caused by thermal effects.

We conclude that these results show that a robotic measurement system can be set up by carefully designing the calibration routine and being able to compensate for, or at least being aware of, systematic changes over the operating time.

Chapter 5

Suggestions for Future Work

Given the fact that repeatability is an important performance criterion that is largely glossed over by many manufactrers, experimental research in this area is very well justified. Our initial experiment was run at 30 % of the maximum joint rates, additional runs at 75 % and 10 %.

The measurement sequence should be reworked so that only one motor is used, thereby providing data on the heat-up contribution of each motor. Several runs at different speeds would be necessary.

Experiments should be run using different robots to perform the same cyclic tasks. The Kawasaki Js-10 would be a good candidate since we have one installed in the same laboratory alongside the KUKA KR-15/2.

Investigations into compensation of link length changes should be made. The operating temperature of the robot could be monitored by means of infra-red sensors, thermo-couples, or other temperature sensors. Appropriate thermodynamic models and compensation algorithms would then be required.

To focus our future work on robotic systems we are currently working on the complete measurement system (robot, head, analysis software, robot kinematics and dynamics) by doing development and evaluation of commercially available products and are perpetually refining the approach. Further investigation should be concentrated in two general ways:

1. Basic research into the exact causes of positioning errors. This would involve experiments designed to reveal the contributions of each robot link and joint to the error. Thermal, dynamic, dimension, and system errors would have to be addressed so as to quantify the percentage of positioning error due to each.

Figure 5.1: Cylindrical and complex profile workpieces.

2. Industrial applications. Depending upon the exact application, we foresee two main branches:

   (a) Use of invariance concepts to obtain measurements of a workpiece based upon unambiguous features of the workpiece itself. In this regard, we have developed a procedure that has been successfully tested for obtaining profile measurements of circular cylinders and complex profile workpieces. The measurement system integrates an optical measurement head and a 6-axis KUKA KR-15/2 robot. The objects are shown in Figure 5.1, while measured sections, obtained with a prototype system, are shown in Figures 5.2 and 5.3. The contributions of the different views are marked in different colors.

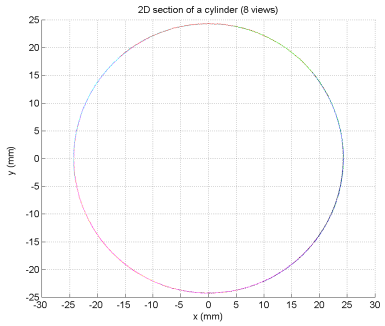

Figure 5.2: Circular cylinder.

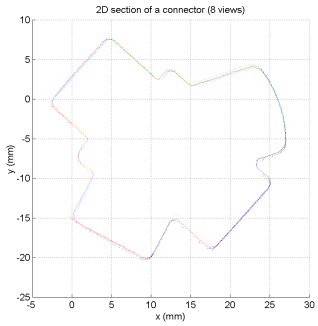

Figure 5.3: Complex profile object.

   (b) Use of registration marks on a measurement work-frame within the robot workspace could be used to perform automatic system calibration any time during the task cycle. The results of the present

experiment demonstrate that it is possible to estimate changes in link length. This information can be used to recalculate the kinematics establishing the true pose of the head. Presently, our work focuses on links 2 and 3 because these links represent the major source of error, but in principle this work can be extended to all links. Indeed, we have successfully tested algorithms to re-identify Denavit-Hartenberg parameters [1] based on small deviations in nominal values.

Bibliography

[1] J.J. Craig. *Introduction to Robotics, Mechanics and Control, second edition.* Addison-Wesley Publishing Co., Reading, Mass., U.S.A., 1989.

[2] Yael Edan, Lea Friedman, Avraham Mehrez, and Leonid Slutski. A three-dimensional statistical framework for performance of robotic systems. *Robotics and Computer-Integrated Manufacturing*, 14:307–315, 1998.

[3] M. Vincze, J.P. Prenniger, and H. Gander. A Laser Tracking System to Measure Position and Orientation of Robot End Effectors Under Motion. *The International Journal of Robotics Research*, pages 305–314, Vol. 13, No. 4, Aug. 1994.

[4] C.H. An, C.G. Atkeson, and J.M. Hollerbach. *Model-based Control of a Robot Manipulator.* The MIT Press, Cambridge, Mass., U.S.A., 1988.

[5] Raziel Riemer and Yael Edan. 3-D Evaluation of Robot Repeatability. *Proc. 27th Israel Conf. on Mech. Eng., Haifa*, pages 580–582, May 19-20, 1998.

[6] Brian Greenway. Robot Accuracy *http://www.wrightind.com/Robot_Accuracy_Paper_WebEdition.htm.*

[7] ISO 9283:1998. Manipulating industrial robots - performance criteria and related test methods.

[8] ISO 9946:1999(E). Manipulating industrial robots - presentation of characteristics.

[9] R. Ofner, P. O'Leary, and M. Leitner. A Collection of Algorithms for the Determination of Construction Points in the Measurement of 3D Geometries via Light-Sectioning. *Wesic '99, 2nd Workshop on European*

Scientific and Industrial Collaboration promoting: Advanced Technologies in Manufacturing, Newport, South Wales, United Kingdom, 1999.

[10] *Physik, Formeln und Gesetze.* VEB Fachbuchverlag, Leipzig, 1988.

[11] Operating Handbook, KR C1 Release 2.2. KUKA Roboter GmbH.